Supplementary Information

Electrical Control of Coherent Spin Rotation of a Single-Spin Qubit

Xiaoche Wang[1], Yuxuan Xiao[2], Chuanpu Liu[3], Eric Lee-Wong[1,4], Nathan J. McLaughlin[1], Hanfeng Wang[1], Mingzhong Wu[3], Hailong Wang[2], Eric E. Fullerton[2,4], Chunhui Rita Du[1,2]

[1]Department of Physics, University of California San Diego, La Jolla, California 92093
[2]Center for Memory and Recording Research, University of California, San Diego, La Jolla, California 92093
[3]Department of Physics, Colorado State University, Fort Collins, Colorado 80523
[4]Department of NanoEngineering, University of California, San Diego, La Jolla, California 92093

Table of content

1. Supplementary Note 1. Characterization of NV-to-sample distances

Nanoscale proximity of NV centers to the patterned magnetic structures is crucial to establishing a strong dipole coupling between NV spins and excited spin waves. We employed NV relaxometry to quantitatively characterize the NV-to-YIG distance for the two NV centers (NV_1 and NV_2) used in our work. The magnetic noise generated by the fluctuation of transverse spin density of YIG at the NV electron spin resonance (ESR) frequencies induces NV spin transitions between $m_s = 0$ and $m_s = \pm 1$ states. The magnitude of such magnetic noise depends on the NV-to-YIG distance d and some other material parameters. The details of the mechanism and the sequences of the NV relaxometry measurements can be found in Ref. 1. Supplementary Figures 1(a) and 1(b) show the measured NV relaxation rate $\Gamma_\pm$ of NV_1 and NV_2 as a function of the external magnetic field B_{ext}. Here, $\Gamma_\pm$ correspond to the relaxation rates of $m_s = 0 \leftrightarrow \pm 1$ transitions, respectively. The measured NV relaxation rates can be theoretically modelled as follows:[1]

$$\Gamma_\pm = C\frac{k_B T}{\hbar\omega_\pm}\int\left(\sin^4(\phi_k) + \cos^2(\theta)\frac{\sin^2(2\phi_k)}{4} + \sin^2(\theta)\sin^2(\phi_k)\right)\frac{Wke^{-2dk}(1-e^{-2t_{\text{YIG}}k})}{\pi\left\{W^2+\left[\omega(k,\phi_k)-\omega_\pm\right]^2\right\}}kdkd\phi_k \qquad \text{(S1)}$$

where C is a constant, T is the temperature, $\omega_\pm$ are the NV ESR frequencies, k_B is Boltzmann constant, θ characterizes the angle of the NV-axis with respect to the normal of the sample surface, d is the NV-to-YIG distance, t_{YIG} is the thickness of the YIG film, $\omega(k, \phi_k)$ is the magnon dispersion function, ϕ_k characterizes the angle between wavevector and in-plane projection of YIG magnetization, and W is the measured linewidth of the ferromagnetic resonance. The dependence on the external magnetic field B_{ext} enters through the NV ESR frequency $\omega_- = 2.87 * 2\pi \pm \gamma B_{\text{ext}}$, and the field-dependent magnon dispersion $\omega(k, \phi_k)$ of the YIG thin film. The measured field-dependence of $\Gamma_\pm$ can be well-fitted by Eq. S1, from which the NV-to-YIG distance d is determined to be 160 ± 6 nm and 330 ± 10 nm for NV_1 and NV_2, respectively.

2. Supplementary Note 2. Theoretical calculations of spin-wave-induced enhancement of NV spin rotation rates

We theoretically calculate the enhancement ratio η of the NV spin rotation rates induced by proximal spin wave modes. We first consider the situation where an NV spin is coupled with the quasi-FMR spin wave mode. Supplementary Figure 2(a) illustrates the cross section of the device structure in our measurements, where w is the width of the microstrip line, x_{NV} and z_{NV} denote the lateral and vertical position of the NV spin relative to the center of the microstrip line, respectively, and I_0 is the magnitude of applied microwave current. The enhancement of spin rotation rate of the NV spin can be expressed as:

$$\eta = \frac{H_{\text{FMR}}}{H_{\text{rf}}}\frac{\sin\theta_{\text{FMR}}}{\sin\theta_{\text{rf}}} \qquad \text{(S2)}$$

where H_{FMR} and H_{rf} characterize the magnetic fields generated by the quasi-FMR spin wave mode and the microstrip line at the NV site, respectively, θ_{sw} characterizes the angle between H_{FMR} and the NV-axis, and θ_{rf} characterizes the angle between H_{rf} and the NV-axis. In our measurement geometry where $x_{\text{NV}} \gg z_{\text{NV}}$, the z-component of H_{rf} can be obtained by Biot-Savart law as follows:

$$H_{\mathrm{rf}} = \frac{I_0}{4\pi w} \ln\left[\left(\frac{w}{2} - x_{\mathrm{NV}}\right)^2 / \left(\frac{w}{2} + x_{\mathrm{NV}}\right)^2\right] \tag{S3}$$

As derived by Clara Mühlherr *et al.* in Ref. 2, H_{FMR} can be expressed as:[2]

$$H_{\mathrm{FMR}} = i\sqrt{2}\,\frac{I_0}{w}\frac{\sin\left(k_x' w/2\right)}{k_x' t}\left[\frac{\gamma\mu_0 M_{\mathrm{s}}\left(\gamma B_{\mathrm{ext}} + \gamma\mu_0 M_{\mathrm{s}} + f\right)}{4\omega^2 - \left(2\gamma B_{\mathrm{ext}} + \gamma\mu_0 M_{\mathrm{s}}\right)^2} e^{-2k_x' t} + \frac{\gamma B_{\mathrm{ext}} + \gamma\mu_0 M_{\mathrm{s}} - f}{2\gamma B_{\mathrm{ext}} + \gamma\mu_0 M_{\mathrm{s}} - 2f}\right] e^{-k_x' z_{\mathrm{NV}}} e^{ik_x' x_{\mathrm{NV}}} \tag{S4}$$

where $k_x' = \frac{2\pi}{w_{\mathrm{YIG}}}$ is the wave number of the quasi-FMR spin wave mode, t is thickness of the YIG strip, $f$is the microwave frequency, γ is the gyromagnetic ratio, μ_0 is the vacuum permeability, B_{ext} is the external field, and M_{s} denotes the saturation magnetization of the YIG pattern. Combing Eqs. S(2) - S(4), η is given by:

$$\eta = 2\sqrt{2}\pi\frac{x_{\mathrm{NV}}}{w}\left|\frac{\sin(k_x' w/2)}{k_x' t}\left(\frac{\gamma\mu_0 M_{\mathrm{s}}\left(\gamma B_{\mathrm{ext}} + \gamma\mu_0 M_{\mathrm{s}} + f\right)}{4f^2 - \left(2\gamma B_{\mathrm{ext}} + \gamma\mu_0 M_{\mathrm{s}}\right)^2} e^{-2k_x' t} + \frac{\gamma B_{\mathrm{ext}} + \gamma\mu_0 M_{\mathrm{s}} - f}{2\gamma B_{\mathrm{ext}} + \gamma\mu_0 M_{\mathrm{s}} - 2f}\right) e^{-k_x' z_{\mathrm{NV}}}\frac{\sin\theta_{\mathrm{FMR}}}{\sin\theta_{\mathrm{rf}}}\right| \tag{S5}$$

Substituting the material and experimental parameters into Eq. (S5): w= 19.6 μm, w_{YIG}= 19.6 μm, t = 20 nm, z_{NV} = 160 nm, x_{NV} = 33.0 μm, $\mu_0 M_{\mathrm{s}}$ = 1646 Oe, k_x' = 0.6283 μm^{-1}, B_{ext} = 200 Oe, f= 2 GHz, and $\frac{\sin\theta_{\mathrm{FMR}}}{\sin\theta_{\mathrm{rf}}} \approx 1$, η is obtained to be 11, in quantitative agreement with the measured experimental value shown in Fig. 2(c) in the main text.

Next, we calculate the enhancement of NV spin rotation rates induced by propagating surface spin wave modes excited by the CPW. Supplementary Figure 2(b) illustrates the cross section of the device structure, where a current of I_0 flows through the central signal line and a current of -I_0/2 flows through the two ground lines. The effective field H_{cpw} generated by the CPW at the NV site is given by the sum of H_{rf} produced by single and ground lines of the CPW:

$$H_{\mathrm{cpw}} = H_{\mathrm{rf}}(x_{\mathrm{NV}}) - \frac{1}{2}[H_{\mathrm{rf}}(x_{\mathrm{NV}} - D) + H_{\mathrm{rf}}(x_{\mathrm{NV}} + D)] \tag{S6}$$

where D characterizes the center-to-center distance of the signal and ground lines, x_{NV} and z_{NV} characterize the lateral and vertical position of the NV center relative to the center of the signal line. Using Biot-Savart law, H_{cpw} can be further expressed as:

$$H_{\mathrm{cpw}}=\frac{1}{4\pi}\frac{I_0}{w}\left\{\begin{array}{l}\ln\left[\left(\frac{w}{2}-x_{\mathrm{NV}}\right)^2/\left(\frac{w}{2}+x_{\mathrm{NV}}\right)^2\right]-\frac{1}{2}\ln\left[\left(\frac{w}{2}-x_{\mathrm{NV}}+D\right)^2/\left(\frac{w}{2}+x_{\mathrm{NV}}-D\right)^2\right]\\-\frac{1}{2}\ln\left[\left(\frac{w}{2}-x_{\mathrm{NV}}-D\right)^2/\left(\frac{w}{2}+x_{\mathrm{NV}}+D\right)^2\right]\end{array}\right\} \tag{S7}$$

Following the similar logic, the effective field H_{sw} generated by the propagating spin wave modes also includes contributions from both signal and ground lines as follows:

$$H_{\mathrm{SW}}=H_{\mathrm{FMR}}(x_{\mathrm{NV}},z_{\mathrm{NV}})-\frac{1}{2}H_{\mathrm{FMR}}(x_{\mathrm{NV}}-D,z_{\mathrm{NV}})-\frac{1}{2}H_{\mathrm{FMR}}(x_{\mathrm{NV}}+D,z_{\mathrm{NV}})=(1-\cos(k_x^{'}D))H_{\mathrm{FMR}} \tag{S8}$$

With the definition of $\eta=\frac{H_{\mathrm{SW}}}{H_{\mathrm{CPW}}}\frac{\sin\theta_{\mathrm{SW}}}{\sin\theta_{\mathrm{CPW}}}$, the enhancement of spin rotation rate of the NV center at the resonant condition of propagating spin wave modes is given by:

$$\eta=\left|\frac{4\sqrt{2}\pi\left(1-\cos k_x^{'}D\right)\frac{\sin\left(k_x^{'}w/2\right)}{k_x^{'}t}\left(\frac{\gamma\mu_0M_{\mathrm{s}}\left(\gamma B_{\mathrm{ext}}+\gamma\mu_0M_{\mathrm{s}}+f\right)}{4f^2-\left(2\gamma B_{\mathrm{ext}}+\gamma\mu_0M_{\mathrm{s}}\right)^2}e^{-2k_x^{'}t}+\frac{\gamma B_{\mathrm{ext}}+\gamma\mu_0M_{\mathrm{s}}-f}{2\gamma B_{\mathrm{ext}}+\gamma\mu_0M_{\mathrm{s}}-2f}\right)e^{-k_x^{'}z_{\mathrm{NV}}}}{\ln\left[\left(\frac{w}{2}-x_{\mathrm{NV}}\right)^2/\left(\frac{w}{2}+x_{\mathrm{NV}}\right)^2\right]-\frac{1}{2}\ln\left[\left(\frac{w}{2}-x_{\mathrm{NV}}+D\right)^2/\left(\frac{w}{2}+x_{\mathrm{NV}}-D\right)^2\right]-\frac{1}{2}\ln\left[\left(\frac{w}{2}-x_{\mathrm{NV}}-D\right)^2/\left(\frac{w}{2}+x_{\mathrm{NV}}+D\right)^2\right]}\frac{\sin\theta_{\mathrm{SW}}}{\sin\theta_{\mathrm{CPW}}}\right| \tag{S9}$$

Substituting the following material and experimental parameters into Eq. (S9): w = 1.5 μm, D = 3.15 μm, t = 100 nm, z_{NV} = 330 nm, x_{NV} = 5.5 μm, μ_0M_{s} = 1697 Oe, k_x' = [k_1, k_2, k_3, k_4] = [0.94, 2.83, 5.13, 6.86] μm^{-1}, B_{ext} = [254.8, 208.5, 173.1, 153.0] Oe, f = [2.15, 2.28, 2.40, 2.44] GHz, and $\frac{\sin\theta_{\mathrm{SW}}}{\sin\theta_{\mathrm{CPW}}}\approx 1$, η is determined to be 150, 111, 47, and 42 for the series of propagating spin wave modes, respectively. The theoretical values obtained from above analytic model are in qualitative agreement with the experimental results shown in Fig. 4(a) in the main text, where η is measured to be 129, 138, 48, and 17, respectively.

3. Supplementary Note 3. Power dependence of NV Rabi oscillation frequencies

The NV Rabi oscillation frequency f_{Rabi} characterizes the amplitude of local microwave magnetic fields at the NV site. When the NV ESR frequency f_- is away from the resonant frequencies of the YIG spin wave modes f_{YIG}, f_{Rabi} is proportional to the amplitude of the microwave magnetic field h_{rf} (h_{cpw}) generated by the stripline (CPW). Because the input microwave power P is proportional to h_{rf}^2, f_{Rabi} is expected to follow a linear dependence on $\sqrt{P}$. When f_- approaches f_{YIG}, the local oscillating magnetic field at the NV site will be dominated by h_{SW} (h_{FMR}) generated by the precessional motion of YIG magnetization. Because $h_{\mathrm{SW}}\propto M_{\mathrm{s}}\sin\Theta = M_{\mathrm{s}}\sin(\frac{\gamma h_{\mathrm{rf}}}{\Delta H})\approx M_{\mathrm{s}}\frac{\gamma h_{\mathrm{rf}}}{\Delta H}$,[3] f_{Rabi} also follows a linear dependence on $h_{\mathrm{rf}}\propto\sqrt{P}$ at the resonant condition of proximal spin wave modes.[4] Here, M_s is saturation magnetization of the YIG strip, Θ characterizes the precessional cone angle of M_s relative to the equilibrium position, γ is gyromagnetic ratio, and ΔH is the linewidth of YIG spin wave modes. Supplementary Figure 3 shows f_{Rabi} measured as a function of $\sqrt{P}$ when $f_- = f_{\mathrm{FMR}}$ and $f_- = f_{\mathrm{FMR}}$ + 50 MHz. In both cases, f_{Rabi} follows the expected linear dependence on $\sqrt{P}$ and exhibits a significantly enhanced slope ($f_{\mathrm{Rabi}}/\sqrt{P}$) at the ferromagnetic resonance (FMR) condition of the patterned YIG strip. Experimentally, we adjusted the input microwave power P to ensure a sufficient signal-to-noise ratio of the measured NV Rabi oscillation spectrum. To normalize the variation of microwave power, we employ $f_{\mathrm{Rabi}}/\sqrt{P}$ as a figure-of-merit to characterize the driving efficiency of the NV spin rotation rate.

4. Supplementary Note 4. Propagating spin waves characterized by spin wave spectroscopy

To further confirm the excitation and propagation of higher order surface spin wave modes, we employed two CPWs fabricated on the patterned YIG waveguide to measure the transmission signals (S_{12}) using a Vector Network Analyzer. The separation s between to the two CPWs is 30 μm and the YIG waveguide is tapered at both ends to avoid potential interference with the reflected spin waves. An external magnetic field B_{ext} is applied along the long-axis of the CPWs to excite the Damon-Eschbach surface spin waves in the YIG waveguide. The input microwave power P is set to be 0 dBm to avoid the nonlinearity of the excited spin waves. Supplementary Figure 4(a) shows the imaginary part of S_{12} measured as a function of B_{ext} and microwave frequency f, where the strong oscillation of the transmission scattering parameter indicates the propagating nature of the excited spin waves with a wavevector of k_1, k_2, and k_3. The absence of the k_4 spin wave mode is due to the significantly reduced amplitude, which is challenging to be detected by spin wave spectroscopy measurements. A linecut of the measured S_{12} map at B_{ext} = -200 Oe [Supplementary Fig. 4(b)] shows the transmission of k_1, k_2, and k_3 spin waves, whose amplitude dramatically decreases as the increase of wavevector, demonstrating a reduced microwave excitation efficiency for the higher order spin wave modes. By extracting the frequency separation Δf of the measured S_{12} spectrum, the group velocity v_g of the propagating spin waves can be determined via equation: $v_g = \Delta f \times s$.[5] For k_1, k_2, and k_3 spin wave modes, v_g is measured to be 870, 690, and 300 m/s, respectively.

5. Supplementary Note 5. Dispersion relationship of propagating spin waves of YIG

In this section, we provide detailed calculations of the magnon dispersion relationship of a magnetic insulator YIG film. Supplementary Figure 5(a) shows a coordinate system for NV-based optical detection of magnetic resonance (ODMR) measurements, where an external magnetic field B_{ext} lies in the y-z plane, θ and θ_{M} characterize the angle of B_{ext} and the static magnetization M_s of the YIG thin film relative to the z-axis, respectively. Introduced by Kalinikos et al., the dispersion relationship of YIG spin wave modes can be calculated through the equation as follows:[6]

$$\omega(k, \phi_k) = \sqrt{\left(\gamma B_{\mathrm{M}} + \frac{D_s}{\hbar} k^2\right)\left(\gamma B_{\mathrm{M}} + \frac{D_s}{\hbar} k^2 + \gamma \mu_0 M_s F(k, \phi_k)\right)} \tag{S10}$$

where γ is the gyromagnetic ratio, $\hbar$ is the reduced Planck constant, B_{M} is the internal field including contributions from B_{ext} and the demagnetizing field $\mu_0 M_s \cos(\theta_{\mathrm{M}})$ generated by the out-of-plane component of the YIG magnetization, D_s = 8.458 × 10^{-40} J m^2 is the spin-wave stiffness constant of YIG, μ_0 is the permeability in free space, k and ϕ_k are polar coordinates describing the magnon wavevector **k** shown in Supplementary Fig. 5(a), and

$$F(k,\phi_k) = P(k) + \sin^2(\theta_M)\left(1 - P(k)(1+\cos^2\phi_k) + \gamma\mu_0 M_s \frac{P(k)(1-P(k))\sin^2\phi_k}{\gamma B_M + \frac{D_s}{\hbar}k^2}\right) \quad \text{(S11)}$$

where $P(k) = 1 - \frac{(1-e^{-kt_{\mathrm{YIG}}})}{kt_{\mathrm{YIG}}}$, t_{YIG} is the thickness of the YIG film. θ_{M} and B_{M} can be quantitatively obtained by solving the following equations:

$$B_{\mathrm{M}}\cos(\theta_{\mathrm{M}}) = B_{\mathrm{ext}}\cos(\theta) - \mu_0 M_s\cos(\theta_{\mathrm{M}}) \quad \text{(S12)}$$

$$B_{\mathrm{M}}\sin(\theta_{\mathrm{M}}) = B_{\mathrm{ext}}\sin(\theta) \quad \text{(S13)}$$

For the quasi-FMR spin-wave mode with a wavevector $k \approx 0$, the magnon dispersion is reduced to a simple formal: $\omega_{\mathrm{FMR}} = \gamma\sqrt{B_{\mathrm{M}}(B_{\mathrm{M}} + \mu_0 M_s \sin^2(\theta_{\mathrm{M}}))}$, which agrees well with the measured ODMR spectrum shown in Fig. 1(c) in the main text.

For the higher order propagating surface spin wave modes ($k \neq 0$) excited by the CPW, we first calculate the wavevectors of the individual spin wave modes. Using the same coordinate system shown in Supplementary Fig. 5(a), the CPW sits on the *x*-*y* plane with its long-axis parallel to the *x*-axis and the center of the signal line is set to be $y = 0$. Supplementary Figure 5(b) plots the spatial profile of the *y*- (red curve) and *z*- (blue curve) components of the inhomogeneous magnetic microwave fields B_y (B_z) generated by the CPW. By Fourier transforming the magnetic field distribution of B_y (B_z), Supplementary Fig. 5(c) shows the obtained excitation spectrum of spin wavevectors, where significant excitation peaks at k_1, k_2, k_3, and k_4 that perpendicular to the long-axis of the CPW emerge. Note that the two excitation spectra obtained by Fourier transforming B_y (B_z) are almost the same. Substituting the numerical values of k_1, k_2, k_3, k_4 and ϕ_k=90° into Eqs. S(10) and S(11), the field dispersion curves of the propagating surface spin wave modes are marked by the white dash lines shown in Fig. 3(d) in the main text, which are in excellent agreement with the observed spin wave features in the ODMR map.

6. Supplementary Note 6. Coupling between back volume spin wave modes and an NV center

In addition to the Damon-Eschbach surface spin wave modes, we also applied an external magnetic field B_{ext} perpendicular to the long-axis of the CPW to excite the backward volume spin wave modes and investigate their coupling with an NV center. Supplementary Figure 6(a) shows the measured ODMR map, where a series of backward volume spin wave modes with discrete wavevectors emerge. Substituting the numerical values of k_1, k_2, k_3 and ϕ_k= 0° into Eqs. S(10) and S(11), the field dispersion curves of the backward volume spin modes are marked by the white dash lines, which are in agreement with the observed spin wave features. In contrast to the surface spin wave modes, the resonant frequencies of back volume spin wave modes decrease as the increase of wavevector due to the long-range dipole interaction. Supplementary Figure 6(b) plots the normalized NV Rabi frequency in both low and high magnetic field regimes. We observed a sharp enhancement of $f_{\mathrm{Rabi}}/\sqrt{P}$ when NV ESR frequency f_- meets the resonant condition of the discrete back volume spin wave modes (red points). As a comparison, $f_{\mathrm{Rabi}}/\sqrt{P}$ almost follows a constant value with a significantly reduced magnitude when f_- stays away from the resonant frequencies of spin waves (blue points).

7. Supplementary Note 7. Measurements of spin coherence time of NV centers in NV-YIG hybrid quantum systems

Spin coherence time (T_2) characterizes the time duration of an NV spin qubit being able to perform an operation or experiment without losing its quantum superposition state. It also determines the ultimate sensitivity of an NV-center-based quantum sensing platform. For NV centers contained in patterned micrometer-sized diamond nanobeams, the characteristic T_2 is mainly determined by magnetic interactions between NV spins and the bath of paramagnetic impurities such as ^{14}N and ^{13}C nuclei. In the studied NV-YIG hybrid quantum systems, the magnetic noise generated by the proximal ferromagnet may also affect the intrinsic spin coherence time of NV spins. Next, we employ the Hanh-echo sequence[7] to quantitatively measure T_2 of NV_1 in the prepared device.

Supplementary Figure 7(a) illustrates the optical and microwave measurement sequence. A green laser pulse was first applied to initialize the NV spin to $m_s = 0$ state followed by a $\pi/2$ microwave pulse with a frequency ω_- applied to rotate the NV spin to the equator of the Bloch sphere, creating a super-positioned state: $|\varphi\rangle = (|0\rangle + |-1\rangle)/\sqrt{2}$. Next, the NV spin will freely evolve on the Bloch sphere and accumulates a phase φ_τ, leading to a new state: $|\varphi\rangle = (|0\rangle + e^{i\phi_{t1}}|-1\rangle)/\sqrt{2}$ after a free evolution time t. Here, $\phi_{t1} = \omega_-\, t = Dt - \gamma B_{\mathrm{ext}}t - \gamma B_{\mathrm{L}}t$, D is the zero-field splitting frequency equaling 2.87 GHz, B_{ext} and B_{L} characterize the external magnetic field and the internal field induced by Larmor precession of ^{13}C nuclei, respectively. A π pulse was then applied followed by another free evolution time t, leading to a new NV spin state: $|\varphi\rangle = (|0\rangle + e^{i(\pi - \phi_{t1} + \phi_{t2})}|-1\rangle)/\sqrt{2}$, where $\phi_{t2} = Dt - \gamma B_{\mathrm{ext}}t - \gamma B'_{\mathrm{L}}t$ and B'_{L} is the effective internal field during the second evolution period. To readout the final NV spin state, we applied a $\pi/2$ microwave pulse with a frequency ω_-. Note that the NV phase accumulation associated with the external magnetic field cancels each other after the two free evolution time periods. Therefore, the final NV spin state is mainly determined by the internal magnetic field B_{L} (B'_{L}) generated by ^{13}C nuclei. When the Larmor precession frequency of ^{13}C nuclei matches $1/2t$, $B_{\mathrm{L}} = -B'_{\mathrm{L}}$ in the two evolution time periods. The total phase accumulation of the NV spin equals $2\gamma B_{\mathrm{L}}t$, giving rise to a periodic oscillation of the measured PL intensity when $2\gamma B_{\mathrm{L}}t$ matches $2n\pi$. To measure the spin coherence time of the NV spin at the YIG FMR condition, Supplementary Fig. 7(b) plots the measured PL intensity as a function of t when $B_{\mathrm{ext}} = 303$ Oe ($f_- = f_{\mathrm{FMR}}$). The evolution time t is chosen to follow $2\gamma B_{\mathrm{L}}t = 2n\pi$ in order to monitor the time-dependent variation of the peak intensity of the measured PL spectrum. By fitting the results to the formula: PL $(t) = \mathrm{A}e^{-t/T_2}$, T_2 of NV_1 is obtained to be 36.74 μs, which is one order of magnitude larger than the reported T_2 of nanodiamonds when they are in proximity to a resonant YIG thin film.[8]

8. Supplementary Note 8. Thermal heating effect associated with electric currents

To minimize the Joule heating effect, we employed synchronized microwave and electrical pulses in the measurements of NV Rabi frequency. The duration time t of the applied microwave and electrical pulses systematically varies from zero to hundreds of nanoseconds. When normalized to the duration time of green laser pulses, the duty cycle of the electrical pulse is less than 10%. As a control measurement, we also performed NV Rabi oscillation measurements with a D. C. electric current. Supplementary Figure 8(a) shows schematic of the measurement sequence.

The temperature increase induced by Joule heat is measured by the zero-field splitting of NV_1: $\Delta T = \frac{D-2.871}{A}$, where $D = \frac{f_+ + f_-}{4\pi\gamma}$, $f_\pm$ correspond to the NV ESR frequencies of $m_s = 0 \leftrightarrow \pm 1$ transitions, and A = -78 kHz/K characterizing the shift of the NV zero-splitting frequency as a function of the temperature.[9] Supplementary Figures 8(b) and 8(c) plot D and ΔT measured as a function of the electric current density J_c in the Pt layer. The measured ΔT is proportional to J_c^2 indicated by the blue fitting curve, which is expected for Ohmic dissipation. Note that when $J_c = 1.0 \times 10^{11}$ A/m^2, the measured ΔT is approaching 100 K. Supplementary Figure 8(d) shows the normalized NV Rabi frequency $f_{\mathrm{Rabi}}/\sqrt{P}$ measured at $J_c = 0$ and $J_c = \pm 5.0 \times 10^{10}$ A/m^2, which clearly deviates from the theoretical predication based on the spin-orbit torque (SOT) model shown in Fig. 2(d) in the main text. We notice that $f_{\mathrm{Rabi}}/\sqrt{P}$ measured at both positive and negative electric current densities ($J_c = \pm 5.0 \times 10^{10}$ A/m^2) are smaller than the zero-current case, which is attributable to the Joule-heat-induced decrease of M_s and the oscillating fields generated by the precesional motion of YIG magnetization.

References:

1. Du, C. H. *et al.* Control and local measurement of the spin chemical potential in a magnetic insulator. *Science* **357**, 195 (2017).
2. Mühlherr, C. Shkolnikov, V. O. & Burkard G. Magnetic resonance in defect spins mediated by spin waves. *Phys. Rev. B* **99**, 195413 (2019).
3. Czeschka, F. D. *et al.* Scaling behavior of the spin pumping effect in ferromagnet-platinum bilayers. *Phys. Rev. Lett.* **107**, 046601 (2011).
4. Robledo, L., Bernien, H., van Weperen, I., & Hanson, R. Control and coherence of the optical transition of single nitrogen vacancy centers in diamond. *Phys. Rev. Lett.* **105**, 177403 (2010).
5. Neusser, S. *et al.* Anisotropic propagation and damping of spin waves in a nanopatterned antidot lattice. *Phys. Rev. Lett.* **105**, 177403 (2010).
6. Kalinikos, B. A., & Slavin, A. N. Ferromagnetic films with mixed exchange boundary conditions. *J. Phys. C: Solid State Phys.* **19**, 7013 (1986).
7. Hahn, E. L. Spin echoes. *Phys. Rev.* **80**, 580 (1950).
8. Andrich, P. *et al*. Long-range spin wave mediated control of defect qubits in nanodiamonds. *npj Quantum Inf.* **3**, 28 (2017).
9. Neumann, P., Jakobi, I., Dolde, F., Burk, C., Reuter, R., Waldherr, G., Honert, J., Wolf, T., Brunner, A., Shim, J. H., Suter, D., Sumiya, H., Isoya, J., & Wrachtrup, J. High-Precision nanoscale temperature sensing using single defects in diamond. *Nano Lett.* **13**, 2738 (2013).

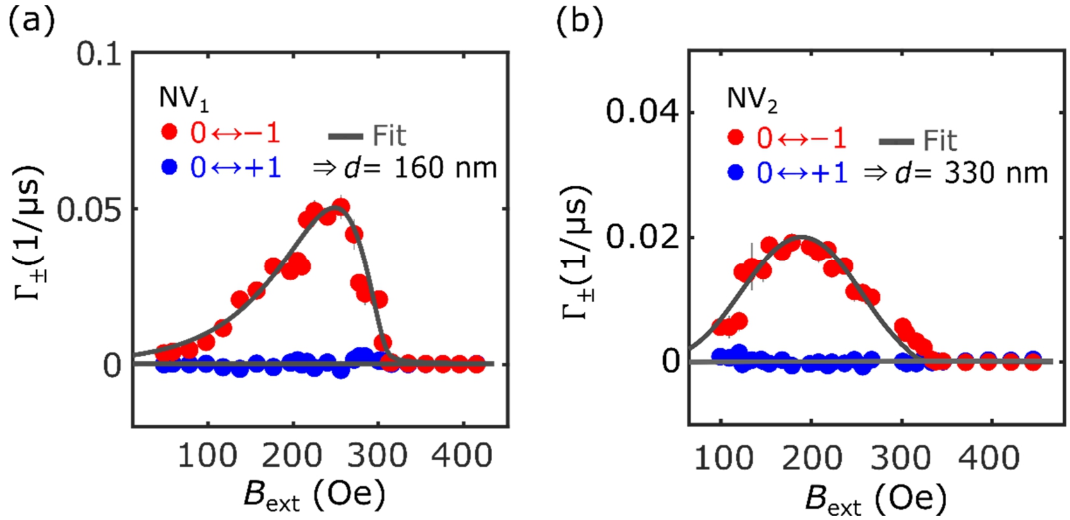

Supplementary Figure 1. Relaxation rates $\Gamma_{\pm}$ of (a) NV$_1$ and (b) NV$_2$ measured as a function of B_{ext}. By fitting the curves to Eq. (S1), the NV-to-YIG distance d is determined to be 160 ± 6 nm and 330 ± 10 nm for NV$_1$ and NV$_2$, respectively.

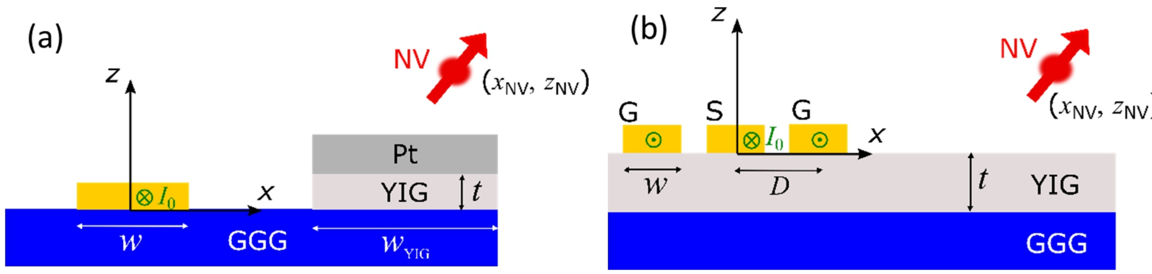

Supplementary Figure 2. Schematic of the cross section view of (a) the type-one YIG-NV/Pt device with a microstrip line and (b) the type-two YIG-NV/Pt device with a coplanar waveguide.

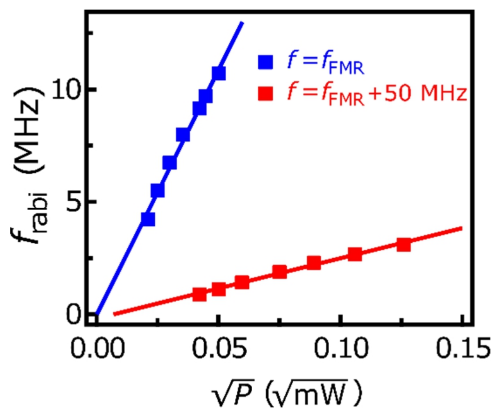

Supplementary Figure 3. NV Rabi oscillation frequency f_{Rabi} measured as a function of the square root of the input microwave power P when $f_{-} = f_{\text{FMR}}$ (blue points) and $f_{-} = f_{\text{FMR}} + 50$ MHz (red points). Blue and red curves are the linear fit of the experimental results.

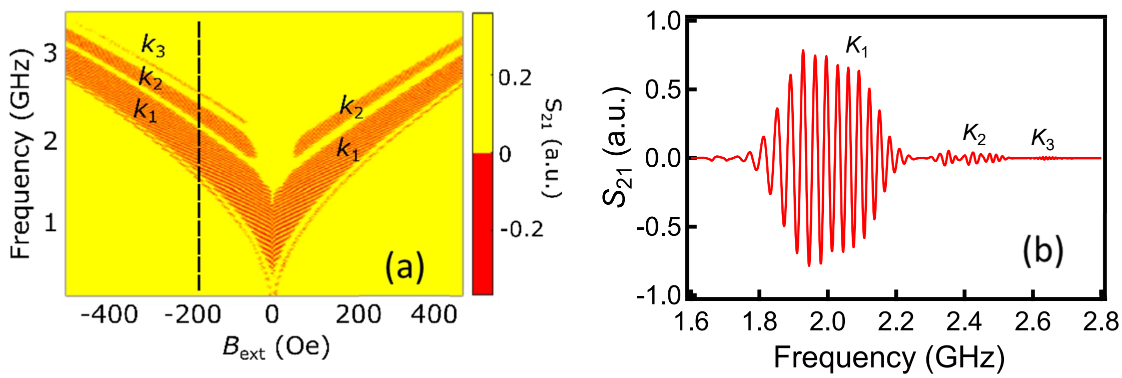

Supplementary Figure 4. (a) Color-coded spin wave transmission spectrum S_{21} measured as a function of B_{ext} and microwave frequency f. (b) A linecut of the S_{21} spectrum at B_{ext} = -200 Oe shows the characteristic oscillation features of the propagating spin wave modes with a wavevector of k_1, k_2, and k_3.

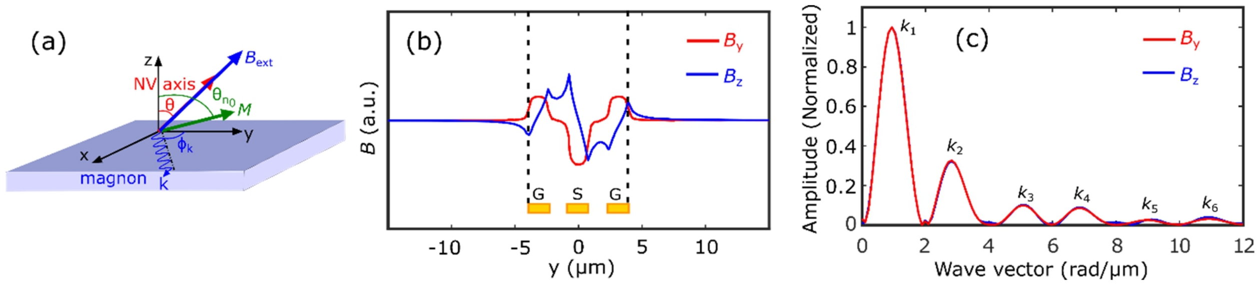

Supplementary Figure 5. (a) The coordinate system used to analyze the magnon dispersion of excited spin waves of YIG. (b) The spatial profile of in-plane and out-of-plane microwave fields B_y and B_z generated by the CPW. The yellow symbols represent the signal and ground lines of a CPW. (c) Spin-wave excitation spectra obtained by Fourier transformation of B_y (red curve) and B_z (blue curve).

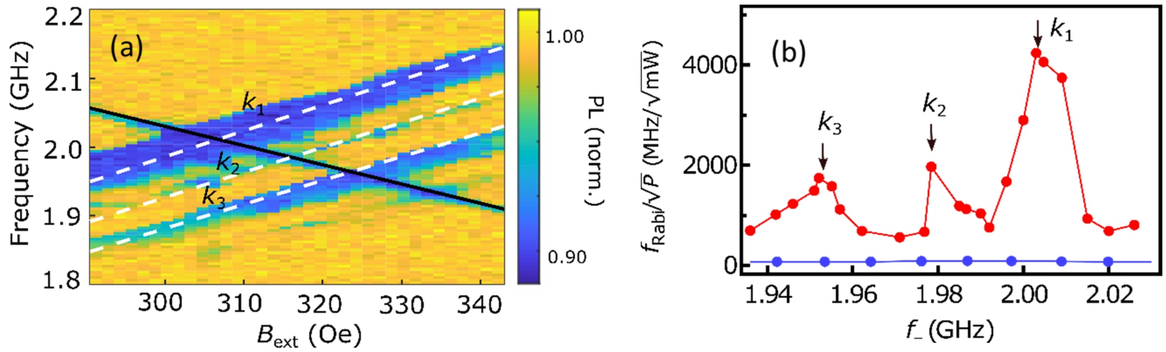

Supplementary Figure 6. (a) An ODMR map measured for back volume spin wave modes excited in YIG. The black straight line corresponds to the NV spin transition between $m_s = 0$ and $m_s = -1$ state and the four white dash lines correspond to the field dispersion curves of back volume spin wave modes with characteristic wavevectors of k_1, k_2, and k_3, respectively. (b) Normalized NV spin rotation rate $f_{\rm Rabi}/\sqrt{P}$ measured as a function of f_- in the low magnetic field (red curve) and high magnetic field (blue curve) regimes.

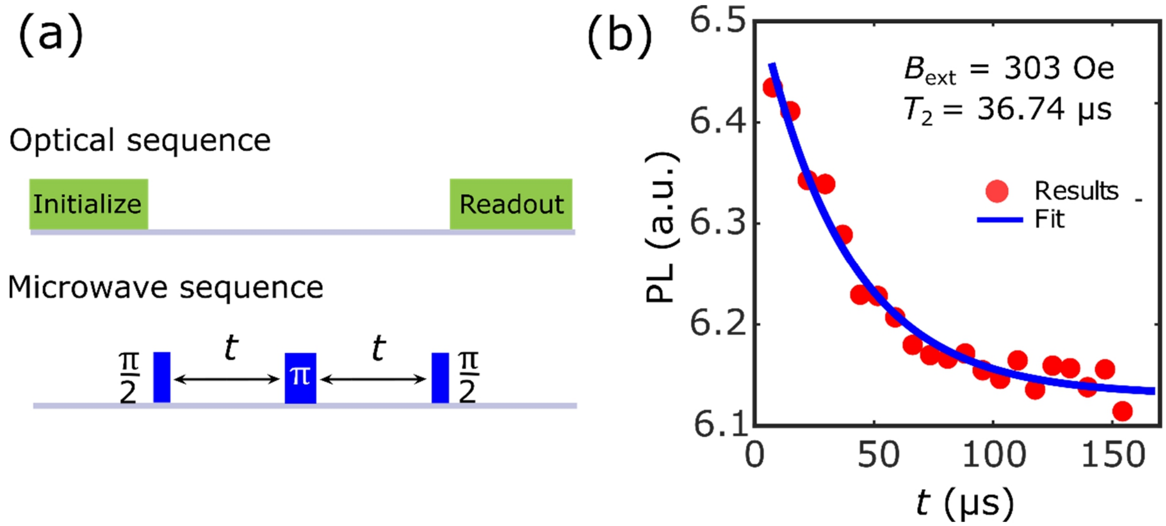

Supplementary Figure 7. (a) Schematic of the Hanh-echo sequence to measure spin coherence time T_2 of NV_1. (b) Time dependence of the measured PL intensity when $B_{ext} = 303$ Oe ($f_- = f_{FMR}$). The free evolution time t is chosen to follow $2\gamma B_L t = 2n\pi$.

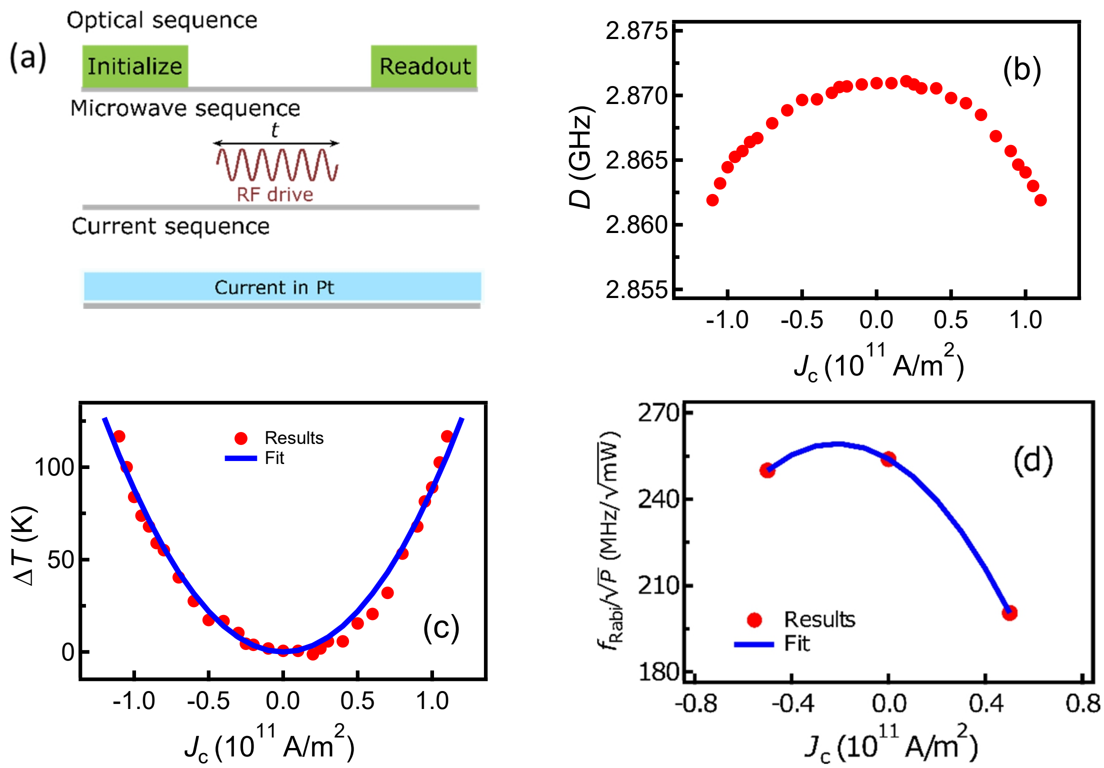

Supplementary Figure 8. (a) Schematic of the NV measurement sequence with a D.C. current. (b) The NV zero-field splitting frequency D measured as a function of the D.C. electric current density J_c. (c) Temperature variation measured (red dots) as a function of J_c. Blue line is a quadratic fit to the experimental results. (d) Normalized NV Rabi frequency $f_{\mathrm{Rabi}}/\sqrt{P}$ measured at $J_c = 0$ and $\pm\ 5 \times 10^{10}$ A/m^2. The blue line is a fit based on a second-order polynomial.